



Comparative analysis of unipolar and bipolar plasma electrolytic oxidation coatings on Al–Mg laminated macro composites

Mohsen RASTEGARI¹, Masoud ATAPOUR¹,
Aboozar TAHERIZADEH¹, Amin HAKIMIZAD², Maryam RAHMATI^{1,3}

1. Department of Materials Engineering, Isfahan University of Technology, Isfahan 84156-83111, Iran;
2. Yekta Mobaddel Pars Co., Science and Technology Campus, Yazd University, Yazd 89158-18411, Iran;
3. Dental Materials Research Center, Dental Research Institute, School of Dentistry, Isfahan University of Medical Sciences, Isfahan 81746-73461, Iran

Received 11 September 2023; accepted 20 May 2024

Abstract: Plasma electrolytic oxidation (PEO) coatings were prepared on Al–Mg laminated macro composites (LMCs) using both unipolar and bipolar waveforms in an appropriate electrolyte for both aluminum and magnesium alloys. The techniques of FESEM/EDS, grazing incident beam X-ray diffraction (GIXRD), and electrochemical methods of potentiodynamic polarization and electrochemical impedance spectroscopy (EIS) were used to characterize the coatings. The results revealed that the coatings produced using the bipolar waveform exhibited lower porosity and higher thickness than those produced using the unipolar one. The corrosion performance of the specimens' cut edge was investigated using EIS after 1, 8, and 12 h of immersion in a 3.5 wt.% NaCl solution. It was observed that the coating produced using the bipolar waveform demonstrated the highest corrosion resistance after 12 h of immersion, with an estimated corrosion resistance of $5.64 \text{ k}\Omega \cdot \text{cm}^2$, which was approximately 3 times higher than that of the unipolar coating. Notably, no signs of galvanic corrosion were observed in the LMCs, and only minor corrosion attacks were observed on the magnesium layer in some areas.

Key words: Al–Mg laminated macro composite; plasma electrolytic oxidation; corrosion behavior; pulsed waveform

1 Introduction

Because of the advantage of low weight and attractive mechanical properties, aluminum–magnesium composites are widely used in various applications, including in the automotive, ship, and aerospace industries [1–3]. Reducing the weight in transportation industries can improve fuel efficiency and decrease greenhouse gas emissions, ultimately decreasing environmental problems such as global warming and air pollution [4]. Unfortunately, by increasing the content of magnesium in these alloys, the Al_3Mg_2 phase is formed along the grain

boundary. Therefore, the weak corrosion resistance of Al–Mg laminated macro composites (LMCs) is the main obstacle to these structures, as it often leads to galvanic and intergranular corrosion, and limits their applications [5–7]. To overcome this limitation, the coating treatments can be considered an essential strategy. Aluminum and magnesium alloys are categorized as valve and active metals, posing a challenge to their electroplating. Electroplated coatings are typically more noble than aluminum and magnesium alloys, thereby restricting their corrosion resistance mechanism to the formation of a physical barrier layer [8,9]. However, such coatings increase the likelihood of

Corresponding author: Maryam RAHMATI, E-mail: mrahmati2011@yahoo.com;
Masoud ATAPOUR, E-mail: m.atapour@cc.iut.ac.ir

[https://doi.org/10.1016/S1003-6326\(24\)66758-0](https://doi.org/10.1016/S1003-6326(24)66758-0)

1003-6326/© 2025 The Nonferrous Metals Society of China. Published by Elsevier Ltd & Science Press

This is an open access article under the CC BY-NC-ND license (<http://creativecommons.org/licenses/by-nc-nd/4.0/>)

localized corrosion in areas where the coating has been compromised. Conventional and traditional anodizing techniques cannot be employed on lightweight metal matrix composites due to the high sensitivity of magnesium layers to acidic media [9,10]. Plasma electrolytic oxidation (PEO) is well-known as an environmentally friendly surface modification technique for improving the corrosion resistance of light alloys, especially magnesium alloys [11,12]. In this regard, many investigations have been conducted to study the microstructure, corrosion, and wear behavior of these alloys after the PEO treatment [13–15]. Thus, the PEO process is expected to be one of the best field-applicable choices for Al–Mg LMCs. It has been well established that an ingrown compact layer and an outgrown porous layer are formed during the PEO treatment. These layers provide a combination of high corrosion and wear resistance [15–17].

The selection of the appropriate waveform is crucial in the PEO process, as it directly affects the quality and properties of the resulting coatings. The current mode can be adjusted to control the thickness of the inner compact layer and the outer porous layer. Alternating current (AC) or direct current (DC), and pulsed unipolar current (PUC) or pulsed bipolar current (PBC) can be used as waveforms [18]. The DC waveform can only produce thin and porous coatings, which reduces the quality of coatings, and is completely contrary to industrial applications [19]. Although PUC has its benefits over DC, such as improved corrosion resistance, its coatings are not satisfactory for aluminum alloys [20,21]. In recent years, PBC has emerged as a promising waveform for producing high-quality coatings compared to PUC, which can be controlled by adjusting the cathodic-to-anodic current ratios to reduce the strong and destructive discharges. The PBC increases polarization on the electrode by creating charged double layers [22]. Therefore, it is expected that using PBC will result in thicker and denser coatings.

The hot extrusion bonding (HEB) process is a severe plastic deformation and a novel solid-state joining technique for the fabrication of Al–Mg LMCs, consisting of at least two different metals or alloys. Various adjustable parameters in this process make it suitable and flexible for manufacturing different macro-composites. Previous studies [23,24] were published to focus on HEB laminated

composites, but only microstructure and mechanical characteristics were reported.

This paper aims to investigate the properties of PEO-coated Al–Mg LMCs, with a particular focus on the effect of unipolar and bipolar waveforms on the characteristics and corrosion resistance of the coatings. To the best of our knowledge, no published study has evaluated the performance of PEO-coated Al–Mg HEB composites. Therefore, the PEO process was performed in an electrolyte that is suitable for both magnesium and aluminum alloys, allowing for the production of a uniform coating on both alloys. The impact of the waveform on the response of cell current density was analyzed, and the phase composition and surface morphology were investigated using X-ray diffraction (XRD) and field emission scanning electron microscopy (FESEM), respectively. The corrosion performance of the coatings was evaluated using potentiodynamic polarization (PDP) and electrochemical impedance spectroscopy (EIS) after immersion in a 3.5 wt.% NaCl solution for 1, 8, and 12 h. Notably, this study found that the coating produced using the bipolar waveform exhibited lower porosity and higher thickness than the unipolar one. The estimated corrosion resistance of the bipolar coating was $5.64 \text{ k}\Omega \cdot \text{cm}^2$ after 12 h of immersion, approximately three times higher than that of the unipolar coating. Furthermore, no signs of galvanic corrosion were observed in the LMCs, and only minor corrosion attacks were observed on the magnesium layer in some areas.

2 Experimental

2.1 Specimen preparation

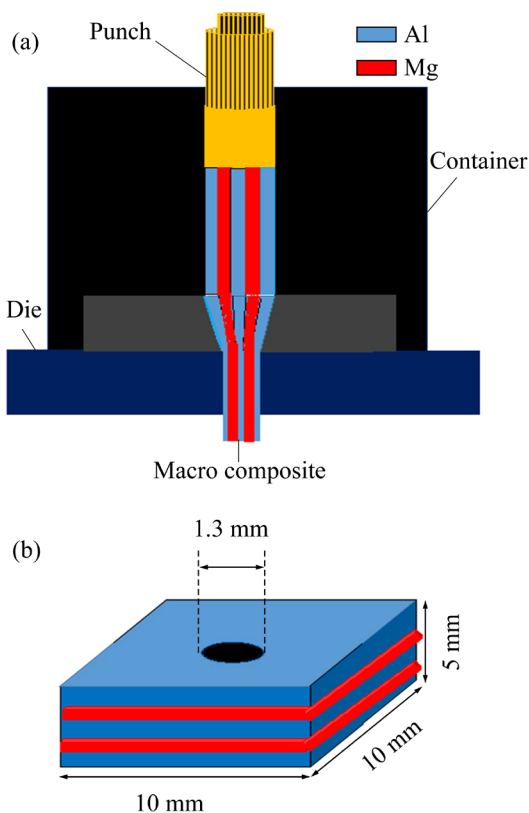
To fabricate Al–Mg LMCs, rolled sheets of 1050 aluminum alloy and AZ31B magnesium alloy were cut in parallel to the initial rolling direction (with dimensions of $50 \text{ mm} \times 50 \text{ mm} \times 5 \text{ mm}$). The chemical compositions of aluminum and magnesium alloys are presented in Table 1. The HEB process was performed using a container made of hot work heat-resistant tool steel, a punch and a holder made of tool steel, and an extrusion die made of heat-treated H13 hot work steel.

The surfaces in contact with the specimen were coated with a mixture of high-temperature lubricant and graphite powder. Before the HEB process, the samples were cleaned with ethyl alcohol

Table 1 Chemical compositions of 1050 Al and AZ31B Mg alloys used in bimetallic macro composite (wt.%)

Alloy	Mg	Al	Cu	Mn	Zn	Ti	Si	Fe
1050 Al	0.05	Bal.	0.48	0.05	0.07	0.04	0.22	0.38
AZ31B Mg	Bal.	3.10	0.02	0.44	0.84	–	–	–

to remove any grease and pollution, ground using SiC abrasive papers to remove the oxide layer, and washed again with acetone. The HEB process was carried out using a 250 t hydraulic press machine at a temperature of 400 °C using heating elements for better bonding and flow during extrusion, as illustrated schematically in Fig. 1(a). The final arrangement of metallic layers in multi-layered macro composites comprised three layers of 1050 aluminum alloy and two layers of AZ31 magnesium alloy all with a thickness of about 1 mm.

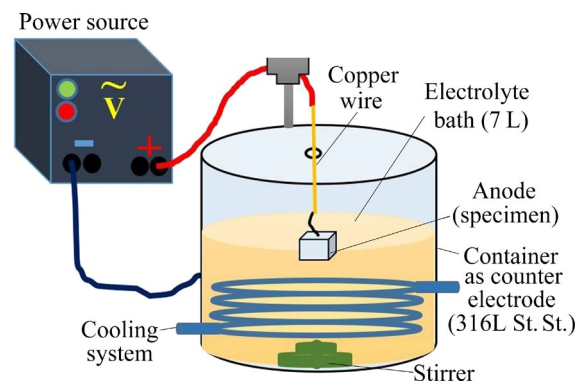
**Fig. 1** Schematics of HEB process (a) and Al–Mg LMCs as substrate (b)

To prepare the specimens for PEO, they were cut using a wire cutter with dimensions of 10 mm × 10 mm × 5 mm. A hole with a diameter of 1.3 mm was drilled at the top of each specimen to connect the copper wire for use as a contact in the PEO process, as depicted schematically in Fig. 1(b).

Before PEO treatment, the cut edges of the specimens underwent grinding using SiC abrasive papers (320[#]–2400[#]), followed by cleaning with ethyl alcohol to remove contaminants and grease.

2.2 PEO process

The PEO treatment was carried out using a silicate-based electrolyte with a composition of 6 g/L Na₂SiO₃, 4 g/L KF, and 8 g/L KOH in a volume of 7 L, as illustrated in Fig. 2. This composition was deemed suitable for coating both aluminum and magnesium alloys, particularly while they were in contact with each other metallurgically.

**Fig. 2** Schematic of PEO process

The electrolyte had a conductivity of 11.79 mS/cm and a pH value of 12.97. A stainless steel container (316 L stainless steel (St. St.)) was employed as a counter electrode for the PEO coating process. A switching power supply equipped with an isolated gate bipolar transistor (IGBT) based pulser capable of delivering potential up to 750 V and current up to 30 A served as the current source.

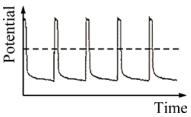
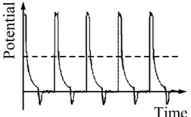
Various waveforms of unipolar (UP) and bipolar (BP) were used with an anodic and a cathodic duty cycle of 10% and a frequency (f) of 1 kHz. The duration of the applied waveforms was 20 min, with an average anodic (positive) current density of 5.6 A/dm². The type of waveforms, waveform plots and electrical parameters utilized in this process are presented in Table 2.

2.3 Coating characterization

The microstructure and morphology of the coated specimens were investigated using a field emission scanning electron microscope (FESEM, FEI model Quanta FEG 450). The chemical composition and elemental maps were evaluated

using an energy-dispersive spectrometer (EDS, EDAX Octane Elite). Elemental analysis of the UP and BP specimens was conducted in two regions on the aluminum and magnesium layers on the cut edges of the LMC specimens. The average thickness and the porosity of the coatings were determined using ImageJ software and metallurgical image processing MIP-student software, respectively. The phase composition of the coated specimens was studied using a grazing incident beam X-ray diffraction (GIXRD, PANalytical (XPert Pro MPD)). The XRD scan was conducted over a 2θ between 10° and 80° by Cu K_α ($\lambda=1.54 \text{ \AA}$) radiation produced at 30 mA and 40 kV. The step size and time per step were set at 0.02° and 48 s, respectively, while the incident beam angle was 5° . The XRD patterns were analyzed using X'Pert high score plus software with PDF2 (Powder Diffraction File for inorganic materials) database.

Table 2 Type of waveforms, electrical parameters, and specimen codes

Waveform	Waveform plot	Electrical parameter				
		t_{on}^+ μs	t_{off}^+ μs	t_{on}^- μs	t_{off}^- μs	f kHz
UP		100	900	0	0	1
BP		100	400	100	400	1

t_{on}^+ , t_{off}^+ , t_{on}^- , and t_{off}^- are the positive pulse duration, the off-duration time after positive pulse, the negative pulse duration, and the off-duration time after negative pulse, respectively

2.4 Corrosion tests

The corrosion behavior of the coatings was assessed using an AMETEK potentiostat/galvanostat (model PARSTAT 2273, AT 2273, Oak Ridge). A three-electrode electrochemical cell was employed for corrosion evaluations. The surface area of the PEO specimens with 2 cm^2 was selected as the working electrode. On the other side, a platinum wire served as the counter electrode, while a saturated Ag/AgCl electrode functioned as the reference electrode. All electrochemical measurements were conducted at room temperature in a 3.5 wt.% NaCl solution with a pH of (6.8 ± 0.1) . Prior to potentiodynamic polarization tests, the

coated specimens were immersed in the electrolyte for 30 min to achieve a stable open circuit potential (OCP). The PDP test was performed from -250 to 1000 mV (vs OCP) at a scan rate of 1 mV/s . The EIS test was carried out after immersion in an aggressive solution for 1, 8, and 12 h. The EIS tests covered a frequency range from 100 kHz to 100 mHz with a peak-to-peak voltage amplitude of $\pm 10 \text{ mV}$ relative to the open circuit potential (OCP). The EIS data were extracted from simulated and fitted tests using Zview software, and the results were presented in Nyquist and Bode-phase plots. To ensure reproducibility, all corrosion tests were repeated twice.

3 Results and discussion

3.1 Voltage–time responses during PEO treatment

Figure 3 shows the variation of voltage versus time using different current modes. It is obvious that relatively similar voltage–time responses are observed for both waveforms. The same trend has been reported in Refs. [19,20,25]. As shown in Fig. 3, the voltage–time diagram has three main stages. The first stage is the conventional and sparking anodization process, which is associated with the fast formation of a primary insulating oxide film. The second one begins with a slight decrease in the voltage rate. At the end of this stage, voltage achieves the dielectric breakdown voltage, and many sparks quickly appear on the surface of the sample, which is strong evidence for the beginning of the oxide layer decomposition. Finally, in the third stage, the potential value remains almost constant [26].

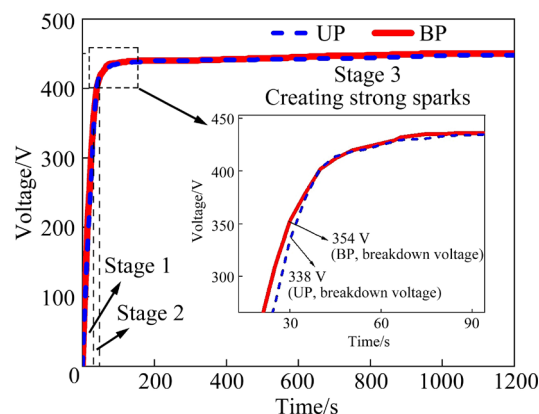


Fig. 3 Responses of cell voltage versus time during PEO process

The noteworthy points in this chart are the breakdown and final voltages. As can be seen, there is a clear difference between the breakdown voltages for the UP and BP. In order to justify this difference, and according to the use of two metals as substrates, it is necessary to investigate the effect of substrate composition on the characteristics of the voltage–time diagrams. It has been reported that substrate composition has a significant effect on ultimate and breakdown voltages. For example, the voltage rises with increasing aluminum content in two-phase alloys, and aluminum prevents high currents caused by substrate dissolution and gas evolution [27]. As seen in Fig. 3, the breakdown voltages for the UP and BP were 338 and 354 V, respectively. It can be concluded that the breakdown voltage of the BP sample was more affected by the current reduction effect of aluminum, which can be explained by the high passivation ability of aluminum in the Al–Mg LMCs. Therefore, voltage rises to accelerate the gas evolution in the second stage. This effect increases the electrical resistance, and the voltage increases according to Ohm's law [20,27]. Other important points are the final voltages, which were 435 and 440 V for the UP and BP samples, respectively. However, the BP sample has a slightly higher final voltage of 5 V compared to the UP sample. The unipolar coating has a higher increasing trend from the breakdown voltage to the final voltage at the end of the process. The slow growth rate causes the coating thickness, and the subsequent final voltage of UP coating to be lower [20]. On the other hand, changing the waveform from unipolar to bipolar affects aluminum substrate more than magnesium [20,22]. As a result, the BP coating becomes thicker, and has a higher final voltage. Most of the growth occurs in the early stages because the difference between the breakdown voltage and final voltage is small, and the voltage increases slowly.

3.2 Characteristics of coatings

3.2.1 Surface morphology

Figure 4 shows the morphologies of the surface and interface of the coatings created on the two-layer alloy using both waveforms at two different magnifications. The FESEM images demonstrate that the morphology of the coatings significantly depends on the type of waveform, micro-discharges that occurred during the PEO

process, and the type of substrate. Specifically, it has been reported [20,21] that the waveform has a considerable effect on the morphology of the coatings created on aluminum alloys (Figs. 4(c) and (f)). In the bipolar waveform compared to the unipolar one, the morphology of the finer and smoother structure has been obtained, which indicates a decrease in the density and intensity of micro-discharges during the coating process [22]. The resulting micro pores in this waveform are smaller. Also, the amount of small and dispersed crater-like structures and oxide granules is more than that of the pancake structure with micro-cracks. The oxide granules were formed by A- and C-type discharges, and a crater-like morphology was created by the rapid solidification of the oxide melt. By comparing Figs. 4(a) and (d), it can be stated that the morphology appears slightly different in both waveforms. The coating formed on the magnesium layer of the macro composite exhibits the net-like morphology. This morphology typically forms on the magnesium alloys treated in silicate-based electrolytes independent of the waveform [28,29]. In the coating obtained with a unipolar waveform, coarser oxide granules with larger micropores, caused the network structure to appear less. As shown in Fig. 4(a), micro-cracks usually appear during the rapid solidification of molten oxide. The main reason for the micro-cracks formation is the thermal stresses owing to different thermal coefficients between coating and substrate [30].

3.2.2 Cross-sectional morphology, porosity, and chemical composition of coatings

Figure 5 shows cross-sectional morphology images of coated specimens with both unipolar and bipolar waveforms on the Al and Mg layers of the macro composite. These images reveal that the coatings generally consist of two distinct layers, namely the porous outer layer and the compact inner layer, as previously reported [20,22,31]. The coatings also exhibit micro-cracks and micro-pores, which are typically attributed to thermal stresses and different types of discharges [32]. The type of discharge is a crucial factor that influences the morphology of PEO coatings [33]. Five types of electrical discharge have been identified for PEO treatment. A-type discharge originates from the oxide/electrolyte interface and the entrapment of gas bubbles, while B-type discharge arises from

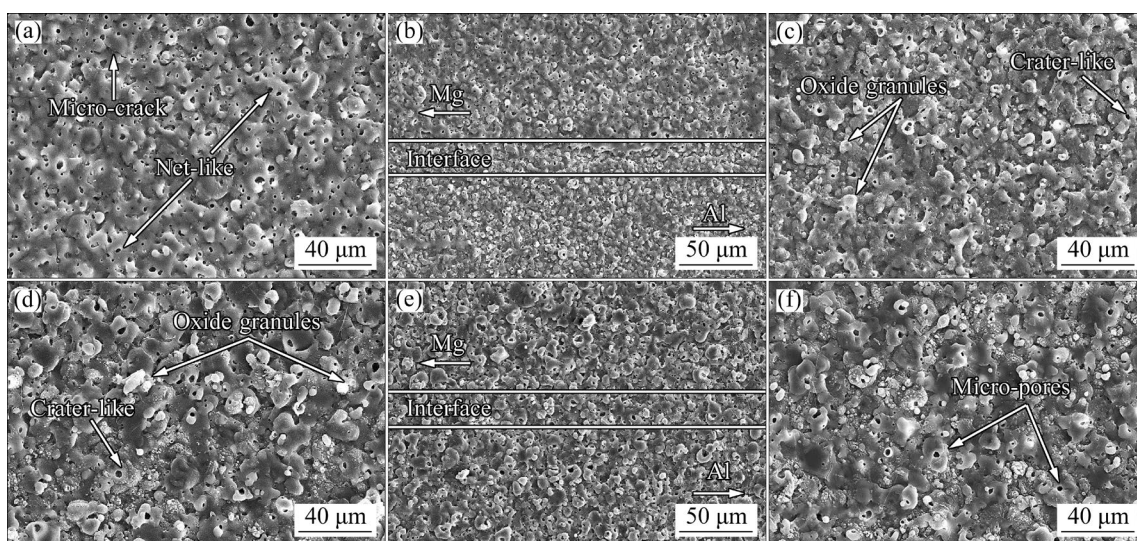


Fig. 4 Surface morphologies using SEM images: (a) UP-Mg; (b) UP-interface; (c) UP-Al; (d) BP-Mg; (e) BP-interface; (f) BP-Al

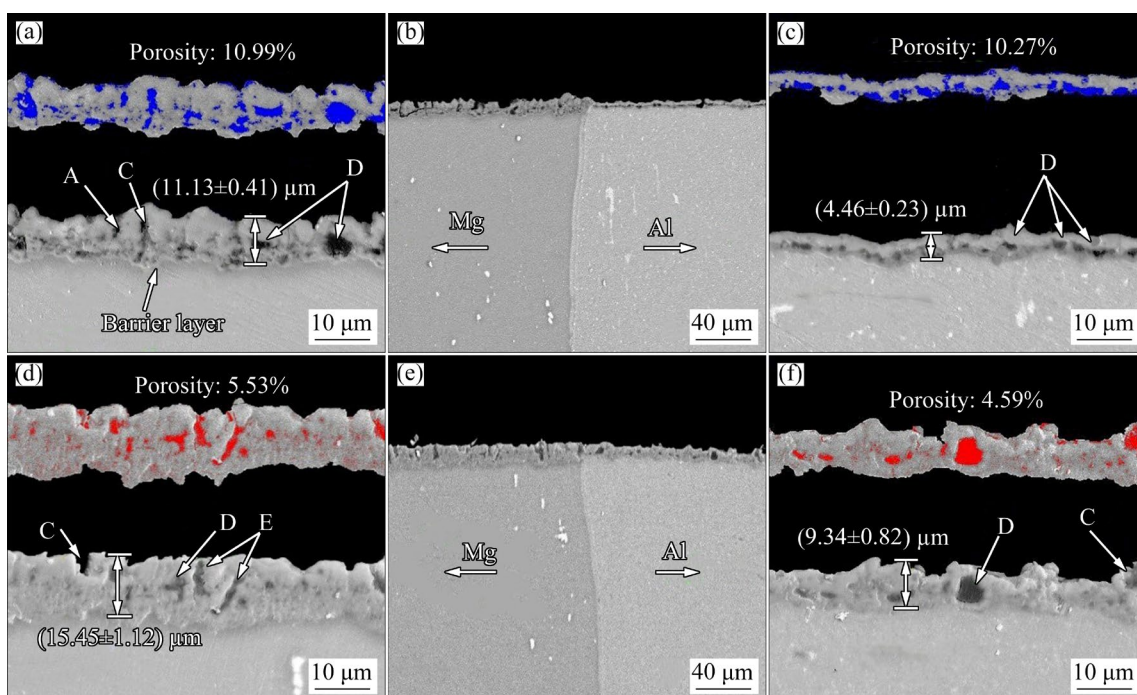


Fig. 5 FESEM images showing cross-sectional morphology: (a) UP-Mg; (b) UP-interface; (c) UP-Al; (d) BP-Mg; (e) BP-interface; (f) BP-Al

the substrate/coating interface, resulting in a deep channel that extends to the substrate. C-type discharge leads to the formation of pores and cracks at the oxide/electrolyte interface (Figs. 5(d) and (f)), whereas D-type discharge typically occurs at the inner/outer oxide layer interface inside large pores, as observed in all samples. The formation of deep channels close to the interface of the inner/outer oxide layer can be attributed to the formation of E-type discharge, as shown in Fig. 5(d). In fact, the

E-type discharges are very similar to the B-type discharges, with a difference that they do not lead to the substrate, and instead are connected to the large internal pores, and are the cause of the pancake structure on the surface of PEO coatings [30,34].

As seen in Figs. 5(b) and (e), a higher coating thickness was observed for the BP on the Mg layer. According to the obtained results, it is clear that, by changing the waveform from unipolar to bipolar, the average thickness increases for both metals

because the cathodic pulse leads to an increase in the thickness with a repair effect [20,22]. Cathodic pulse has a very significant reparative influence on the defects, also it can lead to the sealing of the pores to produce high-quality coatings, which helps the coatings to become thick and compact [35,36].

In addition, the average thickness of the coatings formed on the magnesium was higher than that on aluminum. This case could be due to different coating growth rates of the alloys, also a lower required voltage is needed for magnesium alloys than for aluminum alloys. The applied voltage (435 V) is optimal for magnesium considering the electrolyte and other conditions, while it is definitely low for aluminum, which is at a small distance from the breakdown voltage, and hence it is low to create a thick coating in accordance with Refs. [34,37].

The porosity of the coatings was estimated using MIP software, and the corresponding results are presented in Fig. 5. The coated specimen with the BP waveform exhibited lower porosity compared to UP coating, which is directly attributed to the electrical discharges that occur during the coating process. Figure 5 demonstrates an increase in surface micro-discharges (A- and C-type) for the BP specimen, while deep and destructive micro-discharges (B- and E-type) decrease with this waveform. Additionally, the BP waveform contributes to the reduction and sealing of porosities during the cathodic half-cycle, which leads to an improvement in defects [35]. The disparity in porosity between magnesium and aluminum layers suggests that the voltage applied to the aluminum substrates is below the threshold for strong micro-discharges [22,38].

Figure 6 displays the elemental maps obtained from cross-sections for both waveforms on the Al and Mg layers. The principal elements observed are Mg, Al, O, Si, and F, demonstrating the interaction of elements from both the substrate and electrolyte in the coatings. In addition, Si is uniformly distributed throughout the coatings, with a higher incorporation on the magnesium layer compared to the aluminum layer. This can be attributed to the tendency to form silicate compounds with magnesium, which have a lower melting point (Mg_2SiO_4 at 1910 °C), as opposed to magnesium oxide (2852 °C).

The F element is uniformly distributed in small amounts across each bilayer, regardless of the

applied waveform [39]. The distribution maps of the O element for the Al layer indicate that aluminum can form more oxide compounds compared to magnesium due to the lower melting point of Al_2O_3 (2072 °C) in comparison to MgO (2852 °C). Consequently, aluminum oxides can be sintered more easily in the micro-discharge channels [40].

Table 3 presents the molar fraction obtained from the cross-section analysis of the coatings on the Al and Mg layers, which confirms the higher Si content in the coating of the magnesium layer compared to the aluminum layer, as shown in Fig. 6. It can be clearly seen that almost similar values of Si have been detected on the magnesium when transitioning from the UP waveform to the BP waveform, which shows that the participation of Si is completely independent of the type of waveform for magnesium. However, it significantly increases when using the BP waveform on the aluminum layer coating, and it indicates that the BP waveform is an effective motivation for Si contribution. Furthermore, the F content is higher in the UP waveform compared to the BP waveform, which is attributed to the migration and participation of fluoride ions in anodic pulses under a strong electric field [22].

Consequently, another influential factor in increasing the thickness of the Mg layer is the greater participation of the F element and the formation of MgF_2 compound with a higher Pilling–Bedworth ratio (RPB) of approximately 1.4 compared to MgO (RPB: ~0.8) and Al_2O_3 (RPB: ~1.3) [41–44].

3.2.3 XRD patterns

Figure 7 illustrates the GIXRD results of the coatings grown by UP and BP waveforms. The main phase of the coatings formed on aluminum is Al_2O_3 (ICDD PDF No. 01-073-2294), which is common for the PEO coatings grown on aluminum alloys. The $\text{Al}_{1.7}\text{O}_{2.85}\text{Si}_{0.15}$ phase (ICDD PDF No. 29-0086) was identified as an alumina–silicate phase. However, the mullite ($\text{Al}_6\text{Si}_2\text{O}_{13}$) phase was not detected in the XRD pattern for both waveforms owing to the low incorporation of the silicon element in coatings and the lack of coating condition in terms of current density for the stoichiometric formation of this phase [38]. As can be seen in Fig. 7, the peak associated with MgO

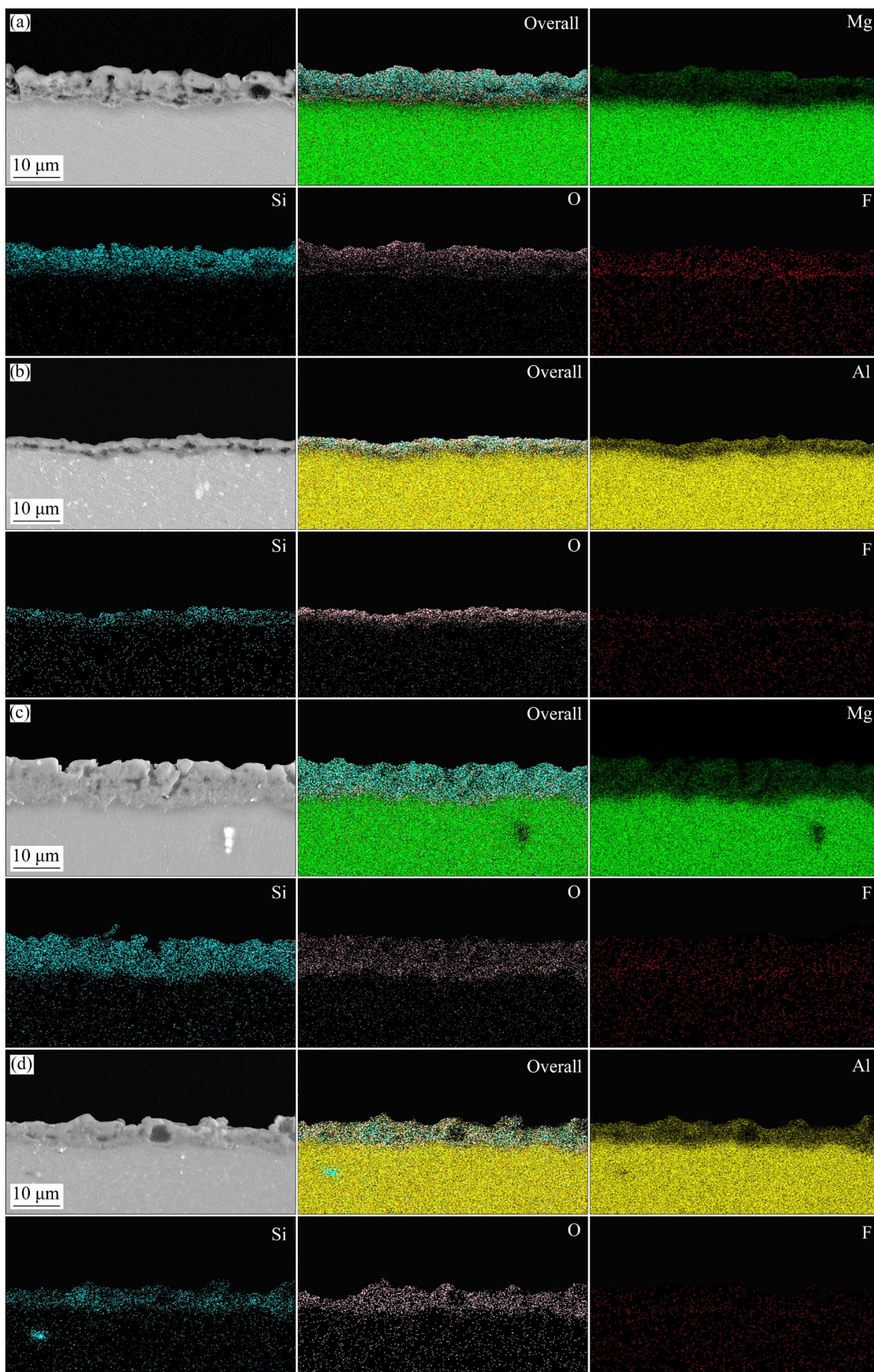
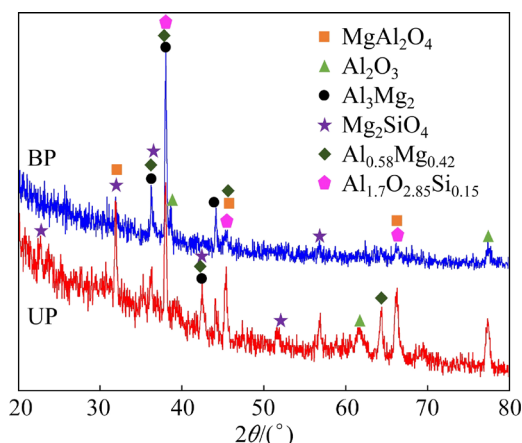


Fig. 6 Elemental maps on cross-sections of coatings: (a) UP-Mg; (b) UP-Al; (c) BP-Mg; (d) BP-Al

Table 3 Elemental compositions of coatings from EDS tests (at.%)

Coating	Mg	Al	O	Si	F	Na	K
UP-Mg	34.9	2.4	39.2	16.3	5.8	0.6	0.8
UP-Al	–	47.8	46.3	4.1	1.5	0.1	0.2
BP-Mg	51.5	3.5	26.4	15.3	1.3	1.1	0.9
BP-Al	–	56.8	32.2	9.8	0.1	0.2	0.9

**Fig. 7** XRD patterns of coatings formed using UP and BP waveforms

was not detected as a common phase for the Mg coatings in the diffraction pattern, which can be justified by the fact that the sharp decrease in the value of MgO is due to the presence of large amounts of aluminum in the macro composite [45]. The significant decrease in MgO is a very strong reason for increasing the amount of Mg_2SiO_4 (ICDD PDF No. 01-1290) as the dominant phase for the Mg in the outer porous layer, which increases using the BP waveform for coating. As can be seen, the intensity of peaks related to the $MgAl_2O_4$ phase increases strongly for the BP waveform compared to the UP waveform. It has been proven that the $MgAl_2O_4$ is formed in the compact inner layer as the main insulating barrier against corrosion [45]. In fact, the BP waveform has a significant effect on the formation of this phase compared to the UP one; therefore, it can be a convincing reason for the high corrosion resistance of BP coatings.

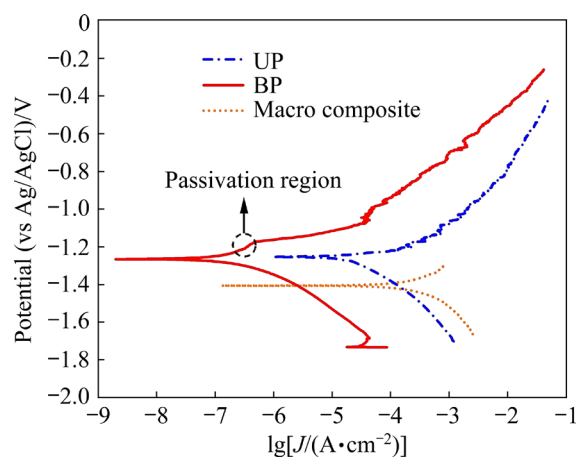
Detecting the intermetallic compounds (stoichiometrically and non-stoichiometrically) in the XRD patterns is very likely due to the presence of two metals. As the temperature increases owing to sparking during the PEO treatment, and according to the Al–Mg phase diagram when both

metals are heated together, Al_3Mg_2 (ICDD PDF No. 01-1132) and $Al_{0.58}Mg_{0.42}$ (ICDD PDF No. 44-1154) are formed as the intermetallic compounds, which can significantly reduce the corrosion resistance of coatings due to galvanic and intergranular corrosion. Generally, the intensity of peaks related to the coatings increases in the BP sample because of the greater thickness and lower porosity percentage [20].

3.3 Corrosion behavior

3.3.1 PDP curves

In order to assess the effectiveness of the coatings in preventing corrosion, the polarization curves of the specimens were analyzed. These curves were obtained after immersing the specimens in a 3.5 wt.% NaCl solution for 30 min to ensure the establishment of stable OCP conditions. Figure 8 illustrates the observed polarization curves. As expected, the substrate exhibited the most negative potential and the highest current density, indicating the lowest corrosion resistance. This can be attributed to both galvanic corrosion between the aluminum–magnesium LMCs, and intergranular corrosion caused by the presence of intermetallic compounds. On the other hand, the Tafel polarization plots of the coated specimens were shifted towards positive potentials, and exhibited lower current densities, indicating an enhanced corrosion resistance due to the presence of the PEO coatings. These coatings not only increased the corrosion performance but also reduced the mobility of charge carriers at the interface between the electrolyte and the substrate [46]. The change in the waveform from

**Fig. 8** Potentiodynamic polarization plots for coated specimens and Al–Mg LMCs substrate as reference

the UP to the BP resulted in a slight leftward shift of the curve in Fig. 8, albeit with a negligible negative potential shift. Consequently, the BP specimen demonstrated a higher corrosion performance compared to the UP one. DEHNAVI et al [47] have shown that the coating morphology will have a more considerable effect on the corrosion behavior than the phase composition and thickness. Also, in many references, the porosity of coatings acts as an essential factor in corrosion resistance [22,32,48].

In addition, micro-crack and micro-pores, as well as other factors related to corrosion resistance facilitate the movement of aggressive ions into the substrate [40]. As can be seen, the BP coating shows the transpassive region, which can be strong evidence for the relatively low porosity of this coating compared to the UP sample.

In fact, the BP specimen provides a key factor in enhancing the corrosion resistance of the coating, which is clearly displayed in the polarization diagram. Here, pitting corrosion is reduced and delayed as a main destructive agent in the BP sample [27]. On the other hand, the high corrosion resistance of the BP sample can be associated with the formation of $MgAl_2O_4$, which can provide a significant protective effect due to the creation of a more compact coating [45]. As a result, the penetration of aggressive chloride ions becomes very slow compared to the UP coating.

3.3.2 Short-term EIS data

The EIS technique was employed to evaluate the corrosion efficiency of the specimens after short-term immersion in a 3.5 wt.% NaCl solution for 1, 8, and 12 h. The Nyquist and Bode-phase plots corresponding to the UP and BP coatings are depicted in Fig. 9. As shown in the inset of Fig. 9, the Al–Mg macro composite substrate displayed the lowest corrosion resistance after 1 h of immersion. At low frequencies, an inductive loop is observed, indicating that the aggressive solution interacts with the magnesium substrate and the interface layers. This inductive behavior can be attributed to hydrogen (H_2) evolution occurring on the surfaces of magnesium and at the interface between the magnesium and aluminum alloy layers. This finding highlights the occurrence of galvanic corrosion between the aluminum and magnesium alloys, suggesting that the substrate is highly susceptible to corrosion. Therefore, it can be concluded that the

macro composite is not safe for prolonged immersion. As previously mentioned, the PEO coating comprises two distinct layers, namely an outer porous layer and an inner compact layer, which is often referred to as the “barrier layer” [18,32]. The outer porous layer exhibits lower mechanical and electrochemical performance, while the dense compact inner layer known as the “functional layer” serves the primary purpose of protecting the metal against wear and corrosion [49]. In the Nyquist plots, the two layers of the PEO coatings are evident as two capacitive loops corresponding to high and low frequencies, representing the porous and dense layers, respectively.

Figure 9(a) illustrates the Bode-phase plots, which reveal the presence of the two distinct layers of the PEO coatings as two humps denoting two time constants. After 1 h of immersion, the BP specimen demonstrates a larger diameter in the Nyquist curve compared to the UP sample, indicating higher corrosion resistance for the BP coating. However, for the UP one, an inductive loop is observed in the low-frequency range, suggesting that the substrate is susceptible to attack by the corrosive solution [22].

Upon examining Fig. 9(b'), it is noticeable that after 8 h of immersion, the humps in the Bode-phase plots for the BP coating merge, and an inductive behavior becomes apparent. This inductive behavior suggests the progression of H_2 evolution on the uncoated surfaces, particularly on the Mg substrate, implying a loss of the coating's ability to protect certain regions of the substrate. An increase in immersion time up to 12 h resulted in the removal of the time constant associated with the porous layer in the UP sample, providing strong evidence for the degradation of the outer porous layer at this specific immersion time. Furthermore, the inner layer exhibited notably weak resistance.

To analyze the impedance data, the equivalent electrical circuits (ECs), as depicted in Fig. 10, were utilized, where R_s represents the uncompensated solution resistance. The CPE_{out} and R_{out} , and CPE_{in} and R_{in} elements denote constant phase elements, and resistances for time constants at high and low frequencies, respectively [28,42]. The adoption of constant phase elements (CPEs) in place of capacitors accounts for electric double-layer non-homogeneity, as well as the presence of micro-cracks and micro-pores within the coatings.

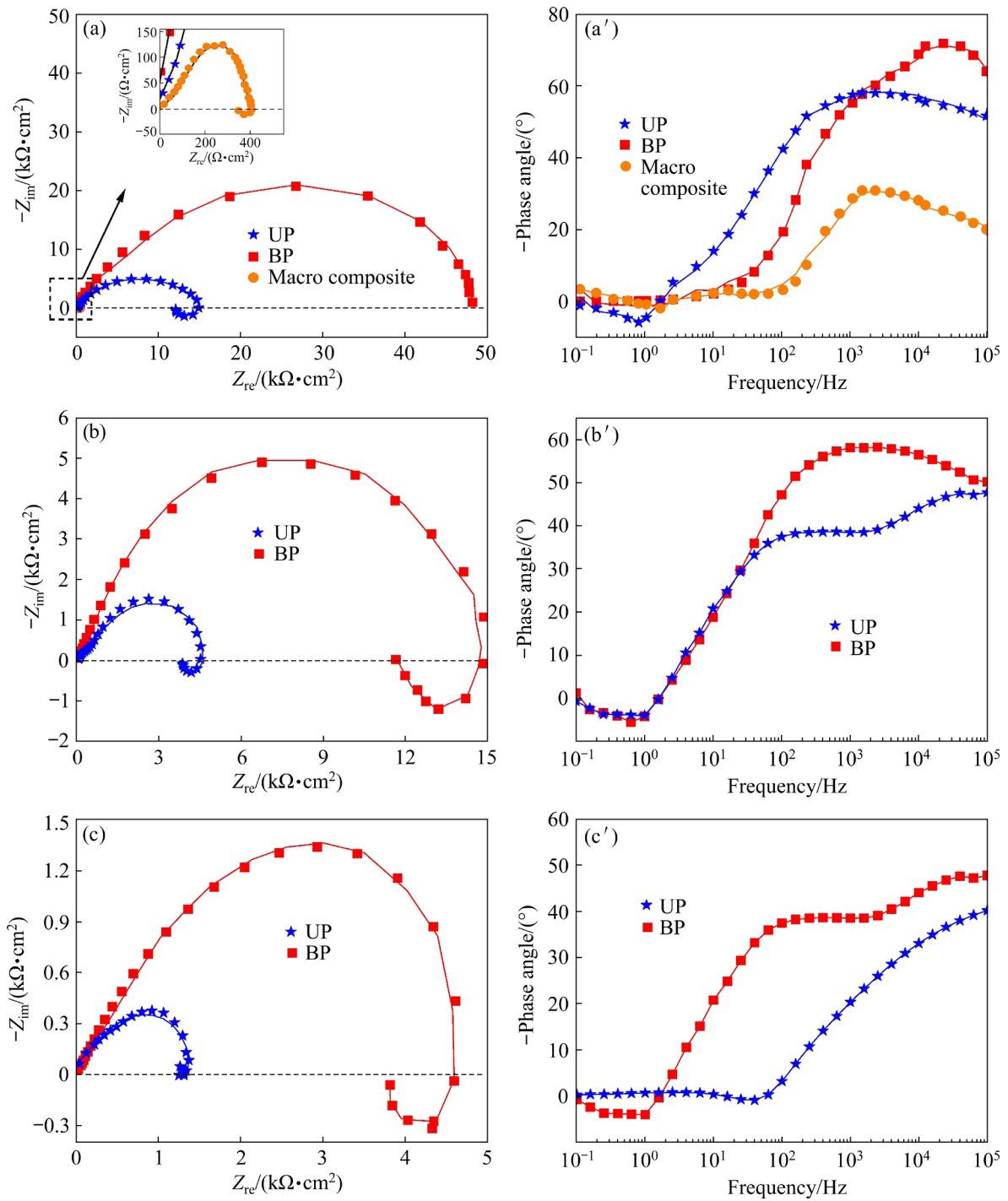


Fig. 9 Nyquist (a, b, c) and Bode (a', b', c') plots of specimens at various immersion time: (a, a') 1 h; (b, b') 8 h; (c, c') 12 h

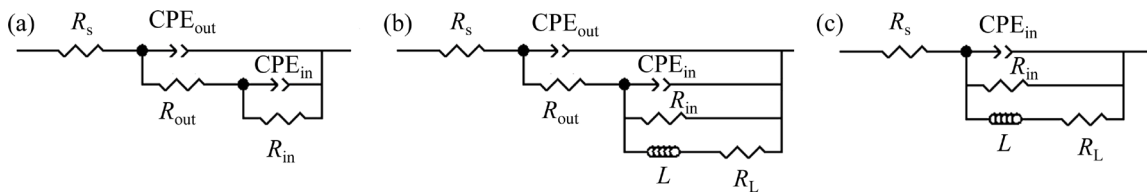


Fig. 10 Equivalent circuits for fitting EIS results: (a) Double-layer; (b) Double-layer with inductive element; (c) Single layer with inductive element

Additionally, L and R_L represent the inductance and inductive resistance, respectively, if applicable [50]. In Fig. 9, the continuous lines represent the fitting results, which yield the most accurate values ($\chi^2 < 0.003$), as reported in Table 4.

After 1 h of immersion, the fitting analysis yielded R_{in} values of 14.19 and 41.87 $\text{k}\Omega \cdot \text{cm}^2$ for the UP and BP specimens, respectively. This considerable difference indicates that the BP coating exhibits 2.9 times higher resistance compared to the UP coating. As depicted in Fig. 9(a), the BP specimen does not exhibit an inductive loop associated with substrate corrosion, which can be attributed to the influence of porosity and thickness on the long-term corrosion resistance of the coatings [22]. Consequently, the corrosion resistance of the BP coating surpasses that of the UP specimen by about 3 times after an immersion period of 12 h.

According to Table 4, the performance of the inner layer weakens with prolonged immersion time, leading to intensive substrate corrosion. However, the R_{out} values for the UP and BP coatings are quite similar after 1 h of immersion (10.34 and 10.48 $\text{k}\Omega \cdot \text{cm}^2$, respectively). After 8 h of immersion, the R_{out} value for the UP coating experiences a substantial decrease, ultimately resulting in a complete loss of corrosion performance after 12 h. For the BP specimen, the decline in R_{out} occurs at a slower rate compared to the UP specimen after 8 h of immersion. However, a sharp reduction in R_{out} is observed after 12 h, indicating a significant decrease in the protective performance of this layer against corrosion. It is worth noting that the R_{in} values obtained from the fitting results are considerably higher than the R_{out} values, as expected. Consequently, the corrosion

behavior of the PEO coatings is evaluated by considering the resistance of the inner layer. In order to gain deeper insights into the corrosion behavior of the coatings, and to analyze the results of the EIS tests following a 12 h immersion period, cross-sectional images of the corroded specimens were examined. Figure 11 shows surface pits observed through field emission scanning electron microscopy (FESEM). These pits serve as indicators of weak areas in the coatings, exhibiting very low corrosion resistance and facilitating direct exposure of the substrate to the aggressive solution [28,50,51]. Specifically, Figures 11(a) and (b) display degradation and prominent pits in the UP coating near the magnesium and aluminum regions, which are attributable to galvanic corrosion occurring between the two metals. Moreover, the phenomenon of pitting corrosion resulting from the attack of aggressive chloride ions on the substrate is evident for both alloys within the UP specimen (Fig. 11(b)).

The simultaneous investigation of the two metals in this study emphasizes the significance of galvanic corrosion as a detrimental factor. The UP coating characterized by low thickness and high porosity exhibits strong discharge traces and the formation of deep channels. Consequently, the aggressive solution can swiftly penetrate the Al/Mg alloy interface. However, the compact structure and low porosity of the BP coating hinder the ingress of aggressive ions, providing enhanced corrosion resistance compared to the UP coating. Pitting corrosion is observed solely on the Mg substrate, which is depicted in Fig. 11(c) for the BP coating. In conclusion, it is evident that porosity plays a crucial role in influencing the corrosion resistance of the coatings.

Table 4 Electrical elements obtained after fitting EIS data using Zview software for UP and BP coatings

Coating	Immersion time/	Outer layer			Inner layer		Inductive response		
		$\text{CPE}_{out}/$ ($\mu\text{F} \cdot \text{cm}^{-2} \cdot \text{S}^{n-1}$)	n_{out}	$R_{out}/$ ($\text{k}\Omega \cdot \text{cm}^2$)	$\text{CPE}_{in}/$ ($\mu\text{F} \cdot \text{cm}^{-2} \cdot \text{S}^{n-1}$)	n_{in}	$R_{in}/$ ($\text{k}\Omega \cdot \text{cm}^2$)	$R_L/$ ($\text{k}\Omega \cdot \text{cm}^2$)	$L/$ ($\text{kH} \cdot \text{cm}^2$)
UP	1	1.57	0.70	10.34	13.58	0.34	14.19	9.6	0.94
	8	0.75	0.72	0.99	14.09	0.53	4.99	11.42	2.62
	12	–	–	–	4.89	0.52	1.65	6.14	1.78
BP	1	0.04	0.80	10.48	0.007	0.84	41.87	–	–
	8	1.79	0.69	8.50	30.34	0.13	12.89	5.15	1.89
	12	0.70	0.73	0.24	10.55	0.58	5.40	11.15	2.18

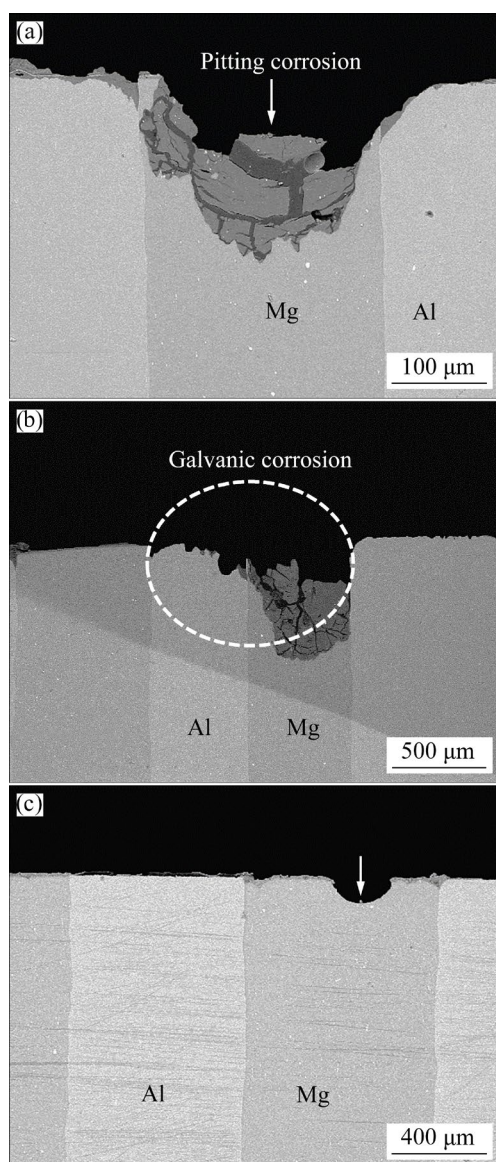


Fig. 11 Cross-sectional morphologies of coated samples after 12 h of immersion in 3.5 wt.% NaCl solution: (a, b) UP; (c) BP

4 Conclusions

(1) The transition from UP to BP waveforms resulted in a notable change in coating morphology, transitioning from pancake-like structures with micro-cracks to a combination of crater-like structures with an increased presence of oxide granules.

(2) The BP coating showed a higher coating growth rate due to the reparative effect of the cathodic pulse on the defects. Additionally, the average thickness of the coatings on Mg alloy is higher than that on Al alloy because of the lower required voltage for oxidation and higher fluoride

content.

(3) The coatings contain Al_2O_3 , $\text{Al}_{1.7}\text{O}_{2.85}\text{Si}_{0.15}$, MgO , Mg_2SiO_4 , and MgAl_2O_4 phases, also Al_3Mg_2 and $\text{Al}_{0.58}\text{Mg}_{0.42}$ are formed as intermetallic compounds because the process is carried out on Al–Mg alloys, and the increase in temperature of micro-sparks causes the formation of these compounds.

(4) The coated specimens were shifted towards positive potentials and exhibited lower current densities, especially the BP, indicating an enhanced corrosion resistance. In addition, the BP coating showed the passivation and transpassivation region that can be attributed to low porosity and greater thickness.

(5) EIS tests demonstrated an enhanced corrosion resistance of $5.64 \text{ k}\Omega \cdot \text{cm}^2$ after 12 h immersion time for the inner layer of the BP coating (approximately 3 times higher than that of the UP sample), highlighting the considerable impact of the waveform on corrosion resistance.

CRedit authorship contribution statement

Mohsen RASTEGARI: Investigation, Data curation, Formal analysis, Resources, Validation, Writing – Original draft preparation, Review & editing; **Masoud ATAPOUR:** Conceptualization, Methodology, Project administration, Supervision, Validation, Visualization, Writing – Review & editing; **Aboozar TAHERIZADEH:** Conceptualization, Methodology, Project administration, Supervision, Validation, Visualization, Writing – Review & editing; **Amin HAKIMIZAD:** Methodology, Data curation, Visualization, Writing – Review & editing; **Maryam RAHMATI:** Investigation, Validation, Methodology, Data curation, Visualization, Writing – Review & editing.

Declaration of competing interest

The authors declare that they have no known competing financial interests or personal relationships that could have appeared to influence the work reported in this paper.

Acknowledgments

Technical support from Plasma Oxide Pars Co., Iran, is gratefully acknowledged.

References

- [1] YANG Hao-kun, QIU Jin, CAO Chi, LI Yuan-dong, SONG Zhao-xi, LIU Wen-jing. Theoretical design and experimental

- study of the interlayer of Al/Mg bimetallic composite plate by solid-liquid cast rolling [J]. *Materials Science and Engineering: A*, 2022, 835: 142677.
- [2] ROUZBEH A, HASHEMI R, SEDIGHI M. Experimental and numerical study of microstructure, mechanical characteristics, and forming limit curve for Al1050/Mg–AZ31B two-layer sheets manufactured via roll bonding technique [J]. *Journal of Alloys and Compounds*, 2023, 942: 169059.
- [3] LIU Ting-ting, SONG Bo, HUANG Guang-sheng, JIANG Xian-quan, GUO Sheng-feng, ZHENG Kai-hong, PAN Fu-sheng. Preparation, structure and properties of Mg/Al laminated metal composites fabricated by roll-bonding: A review [J]. *Journal of Magnesium and Alloys*, 2022, 10: 2062–2093.
- [4] GODJA N C, PAYRITS L, OSTERMANN M, SCHINDEL A, VALTINER M, M. PICHLER C M. Plasma electrolytic oxidation treatments for bimetallic substrates enabling sustainable procedures for automotive painting [J]. *Surface and Coatings Technology*, 2023, 458: 129384.
- [5] SHEN Gu-wei, CHEN Xiao-lin, YAN Jie, FAN Long-yi, YANG Zhou, ZHANG Jin, GUAN Ren-guo. A review of progress in the study of Al–Mg–Zn(–Cu) wrought alloys [J]. *Metals*, 2023, 13: 345.
- [6] ZHANG Di, ZHANG Zhen, PAN Yan-lin, JIANG Yan-bin, ZHUANG Lin-zhong, ZHANG Ji-shan, ZHANG Xin-fang. Current-driving intergranular corrosion performance regeneration below the precipitates solvus temperature in Al–Mg alloy [J]. *Journal of Materials Science & Technology*, 2020, 53: 132–139.
- [7] GUO Cheng, ZHANG Hai-tao, LI Shan-shan, CHEN Ri-xin, NAN Yun-fei, LI Lei, WANG Ping, LI Bao-mian, CUI Jian-zhong, NAGAUMI H. Evolution of microstructure, mechanical properties and corrosion behavior of Al–4Mg–2Zn–0.3Ag (wt.%) alloy processed by T6 or thermomechanical treatment [J]. *Corrosion Science*, 2021, 188: 109551.
- [8] ZHANG Xin, LIU Ai-min, LIU Feng-guo, SHI Zhong-ning, ZHANG Bao-guo, WANG Xu. Electrodeposition of aluminum–magnesium alloys from an aluminum-containing solvate ionic liquid at room temperature [J]. *Electrochemistry Communications*, 2021, 133: 107160.
- [9] GU Chang-dong, LIAN Jian-she, HE Jin-guo, JIANG Zhong-hao, JIANG Qing. High corrosion-resistance nanocrystalline Ni coating on AZ91D magnesium alloy [J]. *Surface and Coatings Technology*, 2006, 200: 5413–5418.
- [10] PAN Fu-sheng, JIANG Bin, HU Yao-bo, WANG Jing-feng, LUO Su-qin. High plasticity magnesium alloys [M]. San Diego: Elsevier, 2022.
- [11] YASUI T, HAYASHI K, FUKUMOTO M. Behaviors of micro-arcs, bubbles, and coating growth during plasma electrolytic oxidation of β -titanium alloy [J]. *Materials*, 2023, 16: 360.
- [12] SALAHSHOURI F, SAEBNOORI E, BORGHEI S, MOSSAHEBI-MOHAMMADI M, BAKHSHESHI-RAD H R, BERTO F. Plasma electrolytic oxidation (PEO) coating on γ -TiAl alloy: Investigation of bioactivity and corrosion behavior in simulated body fluid [J]. *Metals*, 2022, 12: 1866.
- [13] DAVOODI F, ATAPOUR M, BLAWERT C, ZHELUDKEVICH M. Wear and corrosion behavior of clay containing coating on AM 50 magnesium alloy produced by aluminate-based plasma electrolytic oxidation [J]. *Transactions of Nonferrous Metals Society of China*, 2021, 31: 3719–3738.
- [14] DAAVARI M, ATAPOUR M, MOHEDANO M, ARRABAL R, MATYKINA E, TAHERIZADEH A. Biotribology and biocorrosion of MWCNTs-reinforced PEO coating on AZ31B Mg alloy [J]. *Surfaces and Interfaces*, 2021, 22: 100850.
- [15] ATAPOUR M, BLAWERT C, ZHELUDKEVICH M L. The wear characteristics of CeO₂ containing nanocomposite coating made by aluminate-based PEO on AM 50 magnesium alloy [J]. *Surface and Coatings Technology*, 2019, 357: 626–637.
- [16] SELA S, BORODIANSKIY K. Synthesis of ceramic surface on Zr alloy using plasma electrolytic oxidation in molten salt [J]. *Surfaces and Interfaces*, 2023, 36: 102533.
- [17] WU Jia-hao, WU Liang, YAO Wen-hui, CHEN Yan-ning, CHEN Yong-hua, YUAN Yuan, WANG Jing-feng, ATRENS A, PAN Fu-sheng. Effect of electrolyte systems on plasma electrolytic oxidation coatings characteristics on LPSO Mg–Gd–Y–Zn alloy [J]. *Surface and Coatings Technology*, 2023, 454: 129192.
- [18] SANTOS J S, MÁRQUEZ V, BUIJNSTERS J G, PRASERTHDAM S, PRASERTHDAM P. Antimicrobial properties dependence on the composition and architecture of copper–alumina coatings prepared by plasma electrolytic oxidation (PEO) [J]. *Applied Surface Science*, 2023, 607: 155072.
- [19] TRIVINHO-STRIXINO F, DELGADO-SILVA A O, SANTOS J S, RODRIGUES A, MAMBRINI G P, SIKORA M S. Anodization time effect on silver particles deposition on anodic oxide coating over Al produced by plasma electrolytic oxidation [J]. *Plasma*, 2023, 6: 235–249.
- [20] HAKIMIZAD A, RAEISSI K, GOLOZAR M A, LU Xiao-peng, BLAWERT C, ZHELUDKEVICH M L. The effect of pulse waveforms on surface morphology, composition and corrosion behavior of Al₂O₃ and Al₂O₃/TiO₂ nano-composite PEO coatings on 7075 aluminum alloy [J]. *Surface and Coatings Technology*, 2017, 324: 208–221.
- [21] HAKIMIZAD A, RAEISSI K, SANTAMARIA M, ASGHARI M. Effects of pulse current mode on plasma electrolytic oxidation of 7075 Al in Na₂WO₄ containing solution: From unipolar to soft-sparking regime [J]. *Electrochimica Acta*, 2018, 284: 618–629.
- [22] RAHMATI M, RAEISSI K, TOROGHINEJAD M R, HAKIMIZAD A, SANTAMARIA M. Effect of pulse current mode on microstructure, composition and corrosion performance of the coatings produced by plasma electrolytic oxidation on AZ31 Mg alloy [J]. *Coatings*, 2019, 9: 688.
- [23] LI Shuo-shuo, CHEN Liang, TANG Jian-wei, ZHAO Guo-qun, ZHANG Cun-sheng. Microstructure and mechanical properties of hot extruded Mg–8.89Li–0.96Zn alloy [J]. *Results in Physics*, 2019, 13: 102148.
- [24] WOJTASZEK M, ZYGUŁA K. Manufacturing and properties of Al–Al alloy bimetallic composites obtained from powders by hot extrusion [J]. *Composites Theory and*

- Practice, 2022, 2022: 211–218.
- [25] JANGDE A, KUMAR S, BLAWERT C. Evolution of PEO coatings on AM50 magnesium alloy using phosphate-based electrolyte with and without glycerol and its electrochemical characterization [J]. *Journal of Magnesium and Alloys*, 2020, 8: 692–715.
- [26] LING Kui, MO Qiu-feng, LV Xiao-yu, QIN Ge-mei, YANG Wei-wei, LI Lin-wei, LI Wei-zhou. Growth characteristics and corrosion resistance of micro-arc oxidation coating on Al–Mg composite plate [J]. *Vacuum*, 2022, 195: 110640.
- [27] SONG Guang-ling, SHI Zhi-ming. Anodization and corrosion of magnesium (Mg) alloys [M]//*Corrosion Prevention of Magnesium Alloys*. Amsterdam: Elsevier, 2013: 232–281.
- [28] TOULABIFARD A, RAHMATI M, RAEISSI K, HAKIMIZAD A, SANTAMARIA M. The effect of electrolytic solution composition on the structure, corrosion, and wear resistance of PEO coatings on AZ31 magnesium alloy [J]. *Coatings*, 2020, 10: 937.
- [29] DUAN Hong-ping, YAN Chuan-wei, WANG Fu-hui. Growth process of plasma electrolytic oxidation films formed on magnesium alloy AZ91D in silicate solution [J]. *Electrochimica Acta*, 2007, 52: 5002–5009.
- [30] HUSSEIN R O, NORTHWOOD D O, NIE X. Processing-microstructure relationships in the plasma electrolytic oxidation (PEO) coating of a magnesium alloy [J]. *Materials Sciences and Applications*, 2014, 5: 124–139.
- [31] HUSSEIN R O, ZHANG P, NIE X, XIA Y, NORTHWOOD D O. The effect of current mode and discharge type on the corrosion resistance of plasma electrolytic oxidation (PEO) coated magnesium alloy AJ62 [J]. *Surface and Coatings Technology*, 2011, 206: 1990–1997.
- [32] CHAHARMAHALI R, FATTAH-ALHOSSEINI A, ESFAHANI H. Plasma electrolyte oxidation of hydroxyapatite-containing coating on AZ31B Mg alloy: Effects of current density and duty cycle [J]. *Journal of Ultrafine Grained and Nanostructured Materials*, 2021, 54: 149–162.
- [33] PEZZATO L, COLUSSO E, CERCHIER P, SETTIMI A G, BRUNELLI K. Production and characterization of photocatalytic PEO coatings containing TiO₂ powders recovered from wastes [J]. *Coatings*, 2023, 13: 411.
- [34] CHENG Ying-liang, XUE Zhi-gang, WANG Qun, WU Xiang-quan, MATYKINA E, SKELDON P, THOMPSON G E. New findings on properties of plasma electrolytic oxidation coatings from study of an Al–Cu–Li alloy [J]. *Electrochimica Acta*, 2013, 107: 358–378.
- [35] RAHMATI M, RAEISSI K, TOROGHINEJAD M R, HAKIMIZAD A, SANTAMARIA M. Corrosion and wear resistance of coatings produced on AZ31 Mg alloy by plasma electrolytic oxidation in silicate-based K₂TiF₆ containing solution: Effect of waveform [J]. *Journal of Magnesium and Alloys*, 2022, 10: 2574–2587.
- [36] WANG Chen-yang, MA Rui-na, DU An, FAN Yong-zhe, ZHAO Xue, CAO Xiao-ming. Growth methods of PEO coatings on 7075 aluminum alloy at two cathodic current densities [J]. *Surface and Coatings Technology*, 2022, 432: 128099.
- [37] HUSSEIN R O, NIE X, NORTHWOOD D O. An investigation of ceramic coating growth mechanisms in plasma electrolytic oxidation (PEO) processing [J]. *Electrochimica Acta*, 2013, 112: 111–119.
- [38] BAHRAMIAN A, RAEISSI K, HAKIMIZAD A. An investigation of the characteristics of Al₂O₃/TiO₂ PEO nanocomposite coating [J]. *Applied Surface Science*, 2015, 351: 13–26.
- [39] CHEN Qi, ZHENG Yun, DONG Shuai, CHEN Xiao-bo, DONG Jie. Effects of fluoride ions as electrolyte additives for a PEO/Ni–P composite coating onto Mg alloy AZ31B [J]. *Surface and Coatings Technology*, 2021, 417: 126883.
- [40] FADAEI H, JAVIDI M. Investigation on the corrosion behaviour and microstructure of 2024-T3 Al alloy treated via plasma electrolytic oxidation [J]. *Journal of Alloys and Compounds*, 2014, 604: 36–42.
- [41] JAMSHIDIPOUR Z, TOORANI M, ALIOFKHAZRAEI M, MAHDAVIAN M. Reducing damage extent of epoxy coating on magnesium substrate by Zr-enhanced PEO coating as an effective pretreatment [J]. *Journal of Magnesium and Alloys*, 2023, 11: 641–656.
- [42] MORENO L, MOHEDANO M, ARRABAL R, MATYKINA E. Development and screening of (Ca–P–Si–F)–PEO coatings for biodegradability control of Mg–Zn–Ca alloys [J]. *Journal of Magnesium and Alloys*, 2022, 10: 2220–2237.
- [43] WU Ting, BLAWERT C, LU Xiao-peng, SERDECHNOVA M, ZHELUDKEVICH M L. Difference in formation of plasma electrolytic oxidation coatings on MgLi alloy in comparison with pure Mg [J]. *Journal of Magnesium and Alloys*, 2021, 9: 1725–1740.
- [44] FINKELSTEIN A, SCHAEFER A, DUBININ N. Aluminum alloy selection for in situ composite production by oxygen blowing [J]. *Metals*, 2021, 11: 1984.
- [45] WEI Fang-fang, ZHANG Wei, ZHANG Tao, WANG Fu-hui. Effect of variations of Al content on microstructure and corrosion resistance of PEO coatings on MgAl alloys [J]. *Journal of Alloys and Compounds*, 2017, 690: 195–205.
- [46] YANG Wei, JIANG Bai-ling, SHI Hui-ying, XIAN Lin-yun. Effects of KMnO₄ on microstructure and corrosion resistance of microarc oxidation coatings on 2024 aluminum alloy [J]. *Journal of Central South University of Technology*, 2010, 17: 223–227.
- [47] DEHNAVI V, SHOESMITH D W, LUAN Ben-Li, YARI M, LIU Xing-yang, ROHANI S. Corrosion properties of plasma electrolytic oxidation coatings on an aluminium alloy—The effect of the PEO process stage [J]. *Materials Chemistry and Physics*, 2015, 161: 49–58.
- [48] FATTAH-ALHOSSEINI A, CHAHARMAHALI R, BABAEI K. Impressive strides in amelioration of corrosion and wear behaviors of Mg alloys using applied polymer coatings on PEO porous coatings: A review [J]. *Journal of Magnesium and Alloys*, 2022, 10: 1171–1190.
- [49] WU Guo-long, LI Lin, SUN Min, WANG Ye, LUO Fang, ZHANG Qun-li, LIU Rong, CHEN Zhi-jun, YAO Jian-hua. Microstructural evolution and biological properties of PEO coating on SLM-prepared NiTi alloy [J]. *Surface and Coatings Technology*, 2023, 452: 129065.
- [50] IMSHINETSKIY I, KASHEPA V, NADARAIA K, MASH-TALYAR D, SUCHKOV S, ZADOROZHNY P, USTINOV

A, SINEBRYUKHOV S, GNEDENKOV S. PEO coatings modified with halloysite nanotubes: Composition, properties, and release performance [J]. International Journal of Molecular Sciences, 2022, 24: 305.

[51] LI Jiao, BAI Huan-huan, FENG Zhi-yuan. Advances in the modification of silane-based sol-gel coating to improve the corrosion resistance of magnesium alloys [J]. Molecules, 2023, 28: 2563.

Al-Mg 层状宏观复合材料表面 单极与双极等离子电解氧化涂层的对比分析

Mohsen RASTEGARI¹, Masoud ATAPOUR¹,
Aboozar TAHERIZADEH¹, Amin HAKIMIZAD², Maryam RAHMATI^{1,3}

1. Department of Materials Engineering, Isfahan University of Technology, Isfahan 84156-83111, Iran;

2. Yekta Mobaddel Pars Co., Science and Technology Campus, Yazd University, Yazd 89158-18411, Iran;

3. Dental Materials Research Center, Dental Research Institute, School of Dentistry,

Isfahan University of Medical Sciences, Isfahan 81746-73461, Iran

摘要: 以 Al-Mg 层状宏观复合材料(LMC)为基体, 采用单极与双极两种波形, 在适用于铝、镁合金的电解液中制备等离子电解氧化(PEO)涂层。采用场发射扫描电子显微镜/能谱仪(FESEM/EDS)、掠入射 X 射线衍射(GIXRD)、电化学分析法(动电位极化和电化学阻抗谱)等对涂层进行表征。结果表明: 与采用单极波形制备的涂层相比, 采用双极波形制备的涂层具有更低的孔隙率和更大的厚度。在 3.5% (质量分数)NaCl 溶液中浸泡 1、8 和 12 h 后的电化学阻抗谱测试发现, 用双极波形制备的涂层耐腐蚀性最好, 12 h 后的腐蚀阻抗为 5.64 kΩ·cm², 比单极波形制备的涂层的腐蚀阻抗约高 3 倍。值得注意的是, 未观察到 LMC 中电偶腐蚀的发生, 仅在镁层局部存在轻微腐蚀现象。

关键词: 铝镁层状宏观复合材料; 等离子电解氧化; 腐蚀行为; 脉冲波形

(Edited by Wei-ping CHEN)